High-Entropy 2D Carbide MXenes: $TiVNbMoC_3$ and $TiVCrMoC_3$

Srinivasa Kartik Nemani, Bowen Zhang, Brian C. Wyatt, Zachary D. Hood, Sukriti Manna, Rasoul Khaledialidusti, Weichen Hong, Michael G. Sternberg, Subramanian K. R. S. Sankaranarayanan,* and Babak Anasori*

Cite This: https://doi.org/10.1021/acsnano.1c02775

ABSTRACT: Two-dimensional (2D) transition metal carbides and nitrides, known as MXenes, are a fast-growing family of 2D materials. MXenes 2D flakes have $n + 1$ ($n = 1-4$) atomic layers of transition metals interleaved by carbon/nitrogen layers, but to-date remain limited in composition to one or two transition metals. In this study, by implementing four transition metals, we report the synthesis of multi-principal-element high-entropy $M_4C_3T_x$ MXenes. Specifically, we introduce two high-entropy MXenes, $TiVNbMoC_3T_x$ and $TiVCrMoC_3T_x$, as well as their precursor $TiVNbMoAlC_3$ and $TiVCrMoAlC_3$ high-entropy MAX phases. We used a combination of real and reciprocal space characterization (X-ray diffraction, X-ray photoelectron spectroscopy, energy dispersive X-ray spectroscopy, and scanning transmission electron microscopy) to establish the structure, phase purity, and equimolar distribution of the four transition metals in high-entropy MAX and MXene phases. We use first-principles calculations to compute the formation energies and explore synthesizability of these high-entropy MAX phases. We also show that when three transition metals are used instead of four, under similar synthesis conditions to those of the four-transition-metal MAX phase, two different MAX phases can be formed (*i.e.*, no pure single-phase forms). This finding indicates the importance of configurational entropy in stabilizing the desired single-phase high-entropy MAX over multiphases of MAX, which is essential for the synthesis of phase-pure high-entropy MXenes. The synthesis of high-entropy MXenes significantly expands the compositional variety of the MXene family to further tune their properties, including electronic, magnetic, electrochemical, catalytic, high temperature stability, and mechanical behavior.

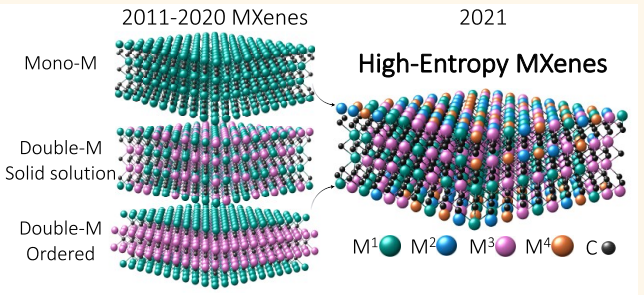

KEYWORDS: *MXenes, 2D materials, multi-principal elements, high-entropy, transition metals, carbides*

MXenes are a large family of two-dimensional (2D) transition metal carbides and nitrides, which were synthesized in 2011.[1,2] MXenes have a chemical formula of $M_{n+1}X_nT_x$ ($n = 1-4$), where a 2D flake is composed of $n + 1$ atomic layers of transition metals from groups 3 to 6 of the periodic table interleaved by a layer of carbon or nitrogen (X) between the M layers.[3,4] In addition, the outer transition metal atomic layers are bonded to surface terminations, such as −O, −F, and −OH.[5] In the past decade, more than 30 MXene compositions have been synthesized, while many more have been studied by computational methods.[6,7] MXenes synthesized to date have exhibited metallic electrical conductivity (up to 20 000 S/cm for $Ti_3C_2T_x$),[8] high in-plane mechanical stiffness (up to 386 ± 13 GPa for $Nb_4C_3T_x$),[9] and impressive catalytic as well as electrochemically active behavior.[3,10] MXenes are synthesized from their precursors, the MAX phases, by selective etching of the A layers, which are generally from groups 13−16 of the periodic table.[11] Most MAX phases that were used for MXene synthesis consist of Al as their A-group element.

MXenes with two transition metals, known as double-transition-metal (DTM) MXenes, have become more prominent in this 2D family since 2015.[12−15] DTM MXenes provide a limitless range of possible compositions of MXenes in the form of random solid solutions of transition metals, where two transition metals randomly occupy the different M layers, which provides control and tunability of MXenes' properties.[15−17] In addition to adding a second transition metal in

Received: April 1, 2021
Accepted: June 8, 2021

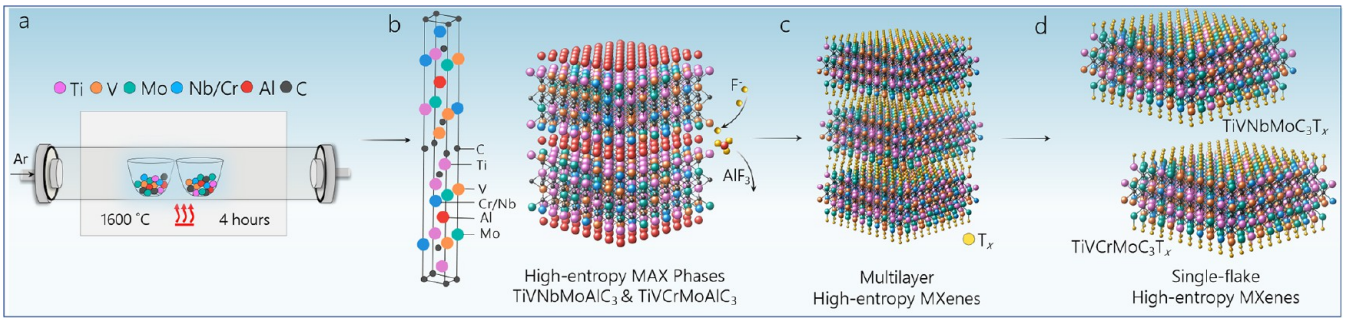

Figure 1. Schematic for the synthesis of high-entropy MAX and MXenes. (a) Reactive sintering of high-entropy MAX phases. Elemental powder mixtures with stoichiometric molar ratios were sintered in alumina crucibles inside of a tube furnace. (b) MAX phase unit cell (left) of M^1 M^2 M^3 M^4AlC_3 with elements Ti (pink), V (orange), Nb or Cr (blue), Mo (green), Al (red), and C (black). The synthesized MAX phases with layered transition metal layers are composed of four transition metal elements, with aluminum (red) and carbon (black) atomic layers in an M_4AlC_3 MAX structure (right). (c) Selective etching of the Al layers by hydrofluoric acid to synthesize multilayer high-entropy MXenes. The surface terminations on the basal planes of MXenes (T_x) are shown in yellow. (d) Delamination of multilayer MXenes is completed *via* organic molecule intercalants, which leads to the formation of single flakes of high-entropy MXenes $TiVNbMoC_3T_x$ and $TiVCrMoC_3T_x$.

previously seen structures of MXene, DTM MXenes also provide unique structures that are not seen in mono-transition-metal MXenes, such as out-of-plane ordered $M_3C_2T_x$ and $M_4C_3T_x$[12] or in-plane ordered M_2CT_x,[13] and a MXene structure of $M_5C_4T_x$ solid solution.[4] DTM MXenes have created avenues for application-specific compositional tailoring that are otherwise impossible in 2D nanomaterials or mono-transition-metal MXenes, such as those predicted to be semiconductive, magnetic, or topological materials in out-of-plane $M_3C_2T_x$ and $M_4C_3T_x$ MXenes.[16,18,19]

Since 2004, multi-principal-element (MPE) high-entropy alloys in bulk 3D crystalline compounds have emerged as promising materials.[20−24] The high-entropy metal alloy concept is a materials synthesis strategy where several (usually five or more) elements are combined in high and near equiatomic concentrations (5−35 at. %) to stabilize a single-phase formation, instead of multiphases of solid solutions with different compositions and crystal structures.[24] They present a vast compositional space with resulting structures and properties that are not observed in single-phase or traditional alloys with only one or two principal elements.[24] The high-entropy alloy concept has been most notably applied to transition metal bulk alloy systems, where exceptional combinations of mechanical properties, thermal stability, and oxidation resistance have been reported. Since 2015, the high-entropy concept has expanded further to 3D crystalline ceramics, where four or more metal elements in equimolar or near equimolar proportions form high-entropy structures with nonmetal elements such as O, C, N, and B.[25−32] Some of the bulk 3D crystalline high-entropy transition metal carbides' properties surpass those of their mono-transition-metal carbides, such as improved hardness, oxidation resistance, wear resistance, and low thermal conductivity.[25,27,33−42] This has led to their application in thermal, corrosive, and extreme-temperature and -pressure environments.[29,30] However, the field of high-entropy transition metal carbides is in its nascent stages of exploration, with only a few studies being reported to-date. Unlike the extensive number of studies on high-entropy 3D crystalline solids, very little has been reported on high-entropy 2D materials. While a few studies explored high-entropy MPE 2D transition metal dichalcogenides,[43,44] to the best of our knowledge, there are currently no reports on high-entropy 2D carbides.

Inspired by the two fast-growing fields of high-entropy compounds and 2D MXenes, we report on successful synthesis of two high-entropy MXenes in this study. To do so, we first synthesized MXene precursors of layered MPE MAX carbides, $TiVNbMoAlC_3$ and $TiVCrMoAlC_3$ phases (Figure 1a,b). These MAX phases are two MPE phases in the potentially large family of high-entropy MAX compositions. After we confirmed the single-phase purity of the high-entropy MAX phases, we exfoliated and delaminated these MAX phases to synthesize $TiVNbMoC_3T_x$ and $TiVCrMoC_3T_x$ (Figure 1c,d) 2D MXenes. In all these synthesized high-entropy phases, the transition metal stoichiometric ratios were retained at 1:1:1:1 (±0.2) for M^1:M^2:M^3:M^4. We verified their synthesizability by calculating the enthalpy of formation for these MAX phase systems using density functional theory (DFT) and a spin-polarized version of the generalized gradient approximation (GGA).[45,46] This development of layered high-entropy MPE MAX phases and their high-entropy MPE MXenes adds an exotic family of MXenes to this large and fast-growing field and provides a method of designing 2D materials with tailored and tunable material properties.

RESULTS AND DISCUSSION

The synthesis of MXenes is a top-down process, which requires making their precursor MAX phases. We synthesized the high-entropy MAX phases by reactive sintering of elemental powders (Figure 1a). Details of the full experimental approach can be found in the Methods Section. Briefly, we first mixed an equimolar ratio of four transition metals M^1, M^2, M^3, and M^4 with Al and C M^1:M^2:M^3:M^4:Al:C in 1:1:1:1:1.1:2.7 stoichiometric ratio to obtain $TiVNbMoAlC_3$ and $TiVCrMoAlC_3$ MAX phases (Figure 1b). We selected our initial starting transition metal combinations in the elemental powders based on the reported stable solid solutions in MAX and MXene phases in earlier theoretical and experimental studies.[1,12,15,16,47,48] By heating the powder mixtures from room temperature to 1600 °C at 3.5 °C/min with a holding time of 4 h under an argon atmosphere (Figure 1a) reactive sintering occurred (Figure S1) and the sintered blocks were milled to obtain fine powders.

First, we used X-ray diffraction (XRD) on the two sintered powders of Ti:V:Nb:Mo:Al:C and Ti:V:Cr:Mo:Al:C and analyzed their spectra to verify the formation of TiVNb-

https://doi.org/10.1021/acsnano.1c02775
ACS Nano XXXX, XXX, XXX−XXX

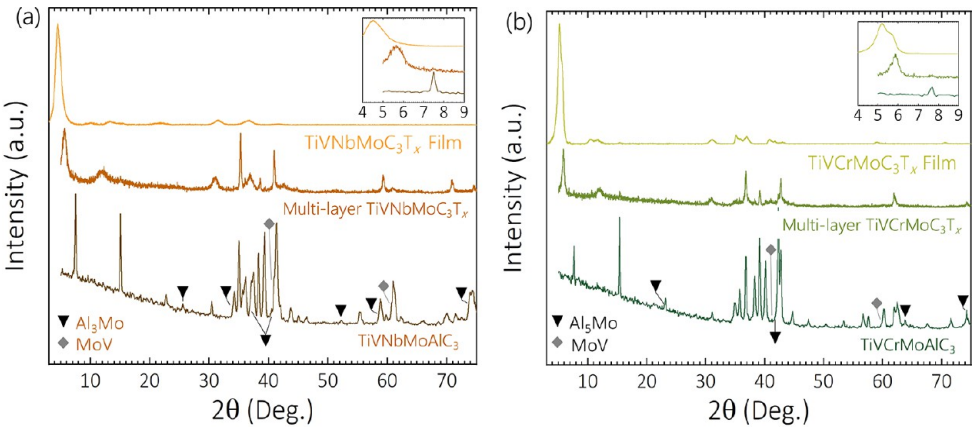

Figure 2. XRD patterns of high-entropy MAX phases and MXenes. (a) XRD patterns of $TiVNbMoAlC_3$ MAX and the resulting $TiVNbMoC_3T_x$ MXenes. (b) XRD patterns of $TiVCrMoAlC_3$ MAX and $TiVCrMoC_3T_x$ MXenes. These plots illustrate the changes in the diffraction pattern from their MAX phase precursor (bottom patterns) to their exfoliated multilayer MXenes (middle patterns) followed by delamination into their single-to-few-flake MXene films (top patterns). Inset in each panel illustrates the shifting of the (002) peak during the evolution from MAX to single-to-few-layer MXene.

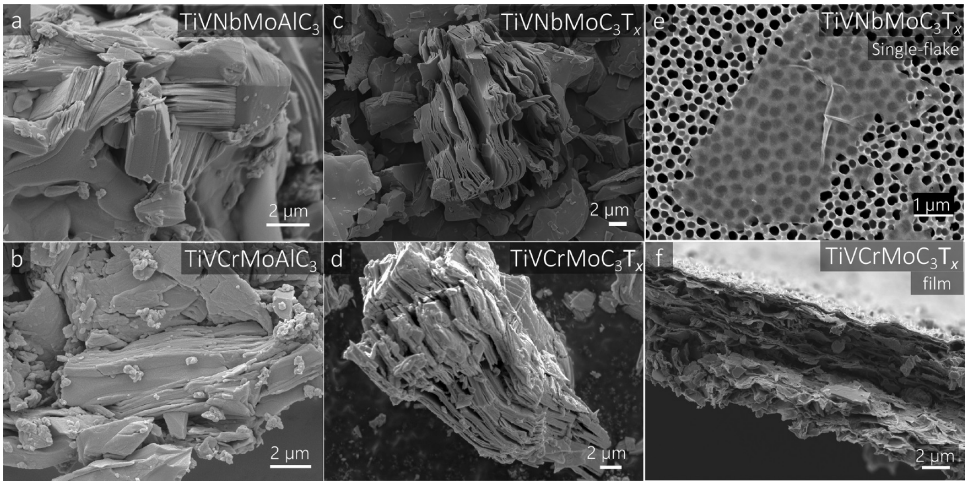

Figure 3. SEM micrographs of high-entropy MAX and MXenes. (a) $TiVNbMoAlC_3$ and (b) $TiVCrMoAlC_3$ showing the layered formation of the carbide structures typical of a MAX phase. (c, d) Etched multilayer MXene powders of (c) $TiVNbMoC_3T_x$ and (d) $TiVCrMoC_3T_x$ with accordion-like morphologies formed due to selective etching of Al layers from MAX phases in high-concentrated HF. (e) Single flake of $TiVNbMoC_3T_x$ MXene on an alumina substrate. (f) Vacuum-assisted filtered film of $TiVCrMoC_3T_x$ MXene.

$MoAlC_3$ and $TiVCrMoAlC_3$ MAX phases (bottom patterns in Figure 2a and b). Using these spectra, we confirmed the presence of M_4AlC_3 MAX phase peaks. Through identification of their characteristic (00*l*) and in-plane peaks, we calculated their *a*-lattice parameters (*a*-LPs) to be 3.038 and 2.970 Å and *c*-LPs of 23.590 and 22.978 Å for $TiVNbMoAlC_3$ and $TiVCrMoAlC_3$, respectively. The identified peaks and lattice parameters of the formed $TiVNbMoAlC_3$ and $TiVCrMoAlC_3$ MAX phases are in good agreement with previously reported non-high-entropy M_4AlC_3 phases.[48,49] After identification of the characteristic M_4AlC_3 diffraction peaks, we focused on evaluating the presence of impurity phases. In this analysis, we identified that common impurities in the synthesis of these MAX phases include small amounts of Al−Mo and Mo−V intermetallics in both $TiVNbMoAlC_3$ and $TiVCrMoAlC_3$. The identification of intermetallic impurities in our system with no other clearly identifiable carbide or oxide impurities *via* XRD analysis indicated that our equimolar high-entropy stabilization synthesis method forms highly pure M_4AlC_3 MAX phases. This is important for their subsequent selective etching and delamination to 2D MXene flakes.

After confirmation of the formation of targeted M_4AlC_3 MAX phases with XRD, we next focused on characterization of the resultant composition of the formed phases using energy-dispersive X-ray spectroscopy (EDS) combined with scanning electron microscopy (SEM). To distinguish the compositions in the resulting MAX phases, we conducted EDS point scans on several MAX particles shown in the SEM micrographs (Figure 3a and b). The average EDS results for the four transition metals in each composition are shown in Table S1 for $TiVNbMoAlC_3$ and $TiVCrMoAlC_3$. These results indicate an equimolar ratio of the four transition metals as Ti:V:Nb:Mo 0.9 ± 0.2:1.1 ± 0.2:1.1 ± 0.2:0.9 ± 0.3 and Ti:V:Cr:Mo ratio of 1.0 ± 0.1:1.1 ± 0.1:1.0 ± 0.1:0.9 ± 0.1. Al content was observed to be a near stoichiometric ratio of 1.1 ± 0.2 in both MAX phases. This is our first confirmation that we have successfully synthesized two MPE MAX phases.

It is important to emphasize the effect of entropy stabilization and the use of four transition metals such as

https://doi.org/10.1021/acsnano.1c02775
ACS Nano XXXX, XXX, XXX−XXX

Ti−V−Nb−Mo or Ti−V−Cr−Mo combinations to synthesize stable, homogeneous, and single-phase M_4AC_3 MAX structures. For example, not all combinations of these elements are found to be stable in DTM MAX phases. DTM MAX phases of Cr and Mo, such as $(Cr, Mo)_4AlC_3$, are predicted to be unstable both in random and ordered solid solution forms.[47] Additionally, for a Nb−Ti-based M_4AlC_3 MAX phase, only $(Nb_{0.8}Ti_{0.2})_4AlC_3$ is reported and no equimolar Nb−Ti-based M_4AlC_3 has been synthesized. The lack of double-transition-metal MAX phases for all the constituent metals suggests that these phases are stabilized because of configurational entropy.

To further investigate the entropy stabilization, we studied the effect of the less-than-equimolar ratio of the four transition metals in $TiVNbMoAlC_3$ and $TiVCrMoAlC_3$. To do so, nine nonequimolar mixtures of the transition metals were prepared by lowering the Mo and Nb content in $(Ti,V,Nb,Mo)_4AlC_3$ and lowering the Cr content in three mixtures in $(Ti,V,Cr,Mo)_4AlC_3$ from 1 to 0.7, 0.4, and 0.1. As for the lower Mo content, we mixed three ratios of Ti:V:Nb:Mo 1.1:1.1:1.1:0.7, 1.2:1.2:1.2:0.4, and 1.3:1.3:1.3:0.1, with Al:C 1.1:2.7 and sintered them at identical conditions to those for the equimolar ratio $TiVNbMoAlC_3$ MAX phase. The resulting compositions were a mix of M_4AlC_3 and M_2AlC MAX phases (Figure S2a) for all three mixtures. For the variable Nb, we prepared three mixtures with ratios of Ti:V:Nb:Mo 1.1:1.1:0.7:1.1, 1.2:1.2:0.4:1.2, and 1.3:1.3:0.1:1.3 with a similar Al:C ratio of 1.1:2.7, and all three mixtures resulted in nonpure M_4AC_3 phases with M_2AC impurities (Figure S2b). Also, for Cr content variation in the $TiVCrMoAlC_3$ MAX phase we mixed elemental powder ratios of Ti:V:Cr:Mo 1.1:1.1:0.7:1.1, 1.2:1.2:0.4:1.2, and 1.3:1.3:0.1:1.3 with Al:C 1.1:2.7, in which again M_2AC peaks were identified as impurity phases in the XRD patterns (Figure S2c). Although all nine powder mixtures were prepared and sintered at identical conditions to the equimolar ratio phases, XRD results indicated undesired M_2AlC MAX phases. While we have not characterized the composition of the undesired multiphases in the nonequimolar mixtures (Figure S2), they can possibly be a mixture of solid solution phases. For example, in $TiVNbMoAlC_3$ M_2AlC may be composed of a previously reported solid solution MAX phase of Nb and V[17,50] and the M_4AlC_3 can contain either Ti−Nb[51] or Ti−V[50] phases. The M_4AlC_3 phase might contain a nonequimolar ratio of all elements as well. Further analysis is needed to understand the stoichiometric ratio of the resulting undesired MAX phases. Regardless of the composition, simultaneous formation of two different MAX phases instead of a single-phase MPE in both $TiVNbMoAlC_3$ and $TiVCrMoAlC_3$ suggests that entropy controls the transition from multiphase to a high-entropy single phase, similar to other high-entropy alloys and ceramics.[24,25] We will discuss the effect of entropy in the computational section of this paper. In general, the presence of a secondary competing MAX phase impurity, such as M_2AlC in this case, creates a challenge in the successful synthesis of MXenes, because the topochemical etching process leads to a mix of two M_2CT_x and $M_4C_3T_x$ MXenes, instead of phase-pure $M_4C_3T_x$ MXenes.

To synthesize high-entropy MXenes, we used the aqueous hydrofluoric acid (HF) etching route, the most common synthesis method for MXenes.[52] To do so, we added powders of $TiVNbMoAlC_3$ and $TiVCrMoAlC_3$ in 48% HF for 4 days at 55 °C to selectively etch Al atomic layers from the high-entropy MAX phases (Figure 1c) followed by repeated washing to a neutral pH (see Methods Section for more details). The reaction pathways of high-entropy MAX phases in aqueous HF and high-entropy MXene formations are presented in the Supporting Information. XRD patterns of the resulting dried powders (Figure 2a,b middle patterns) show a shift of the (002) peak in both phases to 5.65° and 5.84° for multilayer $TiVNbMoC_3T_x$ and $TiVCrMoC_3T_x$, respectively, which indicates an increase in the interflake spacing of 3.85 and 3.64 Å, respectively, compared to their MAX phase precursors. The increase in *c*-LPs and shift in the (00*l*) peak positions are in agreement with previous DTM MXene studies as an indication of exfoliation of M_4AlC_3 MAX phases to $M_4C_3T_x$ MXenes.[48,51,53] The SEM images of the as-etched powders of $TiVNbMoC_3T_x$ and $TiVCrMoC_3T_x$ (Figure 3c,d) show the accordion-like morphologies of multilayer powders, which are usually observed for etched powders with high-concentration HF etching.[3]

To further delaminate the exfoliated high-entropy MXenes into single flakes of 2D MXenes, we used tetramethylammonium hydroxide (TMAOH), which has been implemented for delamination of different MXene compositions.[18,52,54] The delamination of $TiVNbMoC_3T_x$ and $TiVCrMoC_3T_x$ multilayer powders with TMAOH (details in the Methods Section) resulted in black colloidal solutions (Figure S3). These solutions contain single-flake high-entropy MXenes (Figure 3e), which provides evidence of successful delamination of MXenes. By vacuum-assisted filtration of the resulting solutions, we fabricated high-entropy MXene films (Figure 3f and Figure S4). XRD patterns of the filtered films of $TiVNbMoC_3T_x$ and $TiVCrMoC_3T_x$ (Figure 2a and b, top patterns) show only the basal plane peaks (00*l* peaks), which indicates MXene flake restacking during filtration. The most intense (002) peak positions are at 4.51° and 5.22° for $TiVNbMoC_3T_x$ and $TiVCrMoC_3T_x$ films, respectively, which show an increased interflake distance of 7.81 and 5.44 Å as compared to the original MAX *c*-LPs spacing. This increase in interflake distance is in agreement with previous studies analyzing the shifting of the (002) peaks of MXene in single-to-few-flake form.[55] In addition, the (002) peak of $TiVCrMoC_3T_x$ illustrates "double" (002) peaks, where the most intense peak is at 5.22° with a less-intense shoulder peak at 5.65°. These double peaks indicate the partial drying of water molecules from the MXene film.[55] However, $TiVCrMoC_3T_x$ has low-intensity peaks between 31° and 40° 2θ which do not correspond to (00*l*) peaks. These peaks indicate non-basal-plane reflections of MXene, which can be due to the remaining multilayer flakes of MXene particles as seen using cross-sectional SEM methods on the $TiVCrMoC_3T_x$ MXene film (Figure 3f). The absence of non-basal-plane reflections in the $TiVNbMoC_3T_x$ film and the relative low intensity of non-basal-plane peaks in comparison to the highly intense (002) peaks in $TiVCrMoC_3T_x$ indicate that both films are either entirely or mostly, respectively, composed of highly ordered single to few layers of high-entropy MXene flakes.

We next analyzed the composition of the synthesized high-entropy MXenes with EDS combined with SEM on multilayer particles of high-entropy MXenes (Figure 3c,d). The EDS point scans on the multilayer particles of $TiVNbMoC_3T_x$ and $TiVCrMoC_3T_x$ are presented in Table S1, which indicate that the MXene multilayer sheets retain their transition metal stoichiometric ratios of the MAX phase precursors (Figure 3a,b) after HF etching. Our EDS results also show that Mo and Cr molar ratios in the measured multilayer particles are slightly

https://doi.org/10.1021/acsnano.1c02775
ACS Nano XXXX, XXX, XXX−XXX

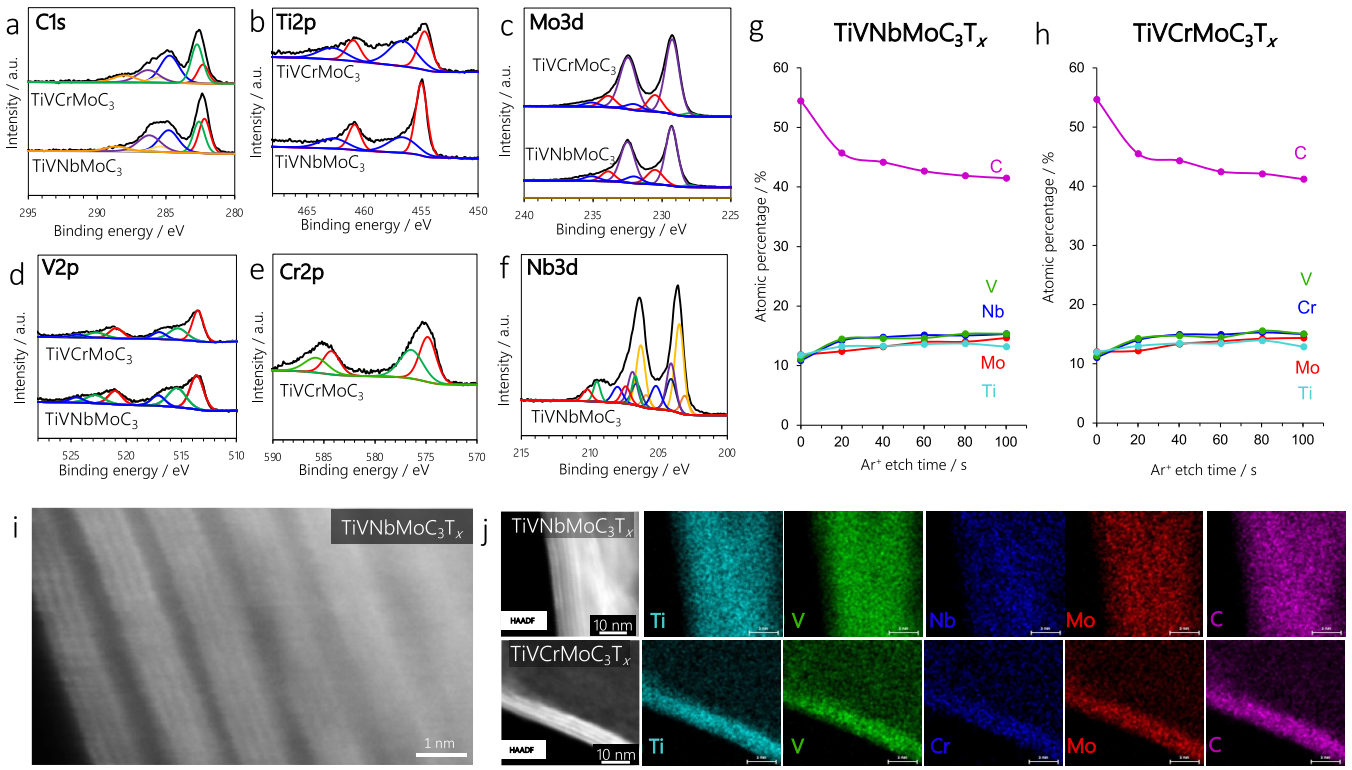

Figure 4. XPS and STEM with EDS results of high-entropy MXenes. (a–f) XPS spectra of $TiVNbMoC_3T_x$ and $TiVCrMoC_3T_x$. (g, h) Atomic % *vs* Ar^+ etching time in XPS for both MXenes. Equiproportional at. % of the principal elements with increased Ar^+ etch rates in XPS indicate the uniform distribution of the atoms in the inner layer of MXenes. (i) High-angle annular dark-field (HAADF) STEM images of $TiVNbMoC_3T_x$ MXene. (j) HAADF STEM combined with EDS results of $TiVNbMoC_3T_x$ (top) and $TiVCrMoC_3T_x$ (bottom) indicating uniform layered morphology and atomic distribution of Ti, V, Nb/Cr, Mo, and C atoms.

lower than those in their respective MAX precursors (Table S1). The slightly lower concentration of Cr in the multilayer high-entropy MXenes may be attributed to relatively weaker Cr–C bonds compared to other M–C bonds[56] and the more reactive nature of Cr-containing MXenes during selective etching.[18] The etching conditions used here, 48% HF for 96 h at 55 °C, are among the harshest conditions used for the synthesis of MXenes.[57] Additionally, while our results indicate favorable entropy stabilization, we cannot rule out the tendency of Mo and Cr to prefer the outer transition metal atomic layers in a MXene 2D flake, as was observed in ordered double-transition-metal MAX and MXene phases.[12,58–63] The possible preferred atomic positions of Mo and Cr can expose them directly to HF during etching, which leads to their relatively higher removal rates while creating their transition metal vacancies in the outer M layers.[64] Future studies are needed to probe any possibility of ordering in these MPE MXenes.

We further analyzed the compositions and chemical bonding within our high-entropy MXenes by conducting X-ray photoelectron spectroscopy (XPS) analysis to evaluate the chemical states as well as the coordination of the transition metals and carbon within the high-entropy $TiVNbMoC_3T_x$ and $TiVCrMoC_3T_x$ MXenes. To gain an average distribution of Ti, V, Nb/Cr, Mo, and C, we set the spot size to 400 μm for all XPS analyses. Figure 4a–f show the XPS high-resolution spectra for the top surface of as-prepared $TiVNbMoC_3T_x$ and $TiVCrMoC_3T_x$ MXenes. The C 1s high-resolution spectra highlight the existence of C–Mo/Ti–T_x, C–Ti/MoT_x, C–C–CH_x, C–O, and COO moieties in both structures. The complex nature of this chemical bonding was also seen in other MXenes, including titanium carbide (*e.g.*, $Ti_3C_2T_x$) and niobium carbide (Nb_2CT_x).[65–67] The Ti 2p regions for both $TiVNbMoC_3T_x$ and $TiVCrMoC_3T_x$ highlight the coordination of Ti as Ti–C and TiO_2 (note that TiO_2 forms due to surface oxidation of the MXene). The V 2p region suggests that V is coordinated *via* V^{2+}/V^{4+} moieties or as V_2O_3, while the Mo 3d region indicates that Mo exists as Mo^{5+}/Mo^{6+}, C–Mo–T_x, and Mo in both structures. For $TiVNbMoC_3T_x$, the Nb coordination is composed of several species, including Nb^0, Nb (I, II, or IV) NbO, Nb^{3+}–O, Nb^{4+}–O, and Nb_2O_5, and while in $TiVCrMoC_3T_x$, the Cr coordinates as Cr^{2+} and Cr^0. We also observed –O and –F groups, which indicate the presence of surface moieties on the basal planes of the MXenes shown in Figure S5. Full details regarding the spectral deconvolutions can be found in Tables S2 and S3.

To further probe the distribution and evaluate the presence of Ti, V, Nb/Cr, Mo, and C in $TiVNbMoC_3T_x$ and $TiVCrMoC_3T_x$, we performed XPS depth profiles with Ar^+ etching (Figure 4g,h). Since the films were exposed to the air and due to possible surface oxidation, without Ar^+ etching XPS is unable to provide reliable data on the composition of the constituent elements. The etching with Ar^+ ions at a rate of 0.05 nm/s enabled removal of surface impurities, and the relative magnitude of the elemental deviation was more apparent after 20–30 s of Ar^+ etching (Figure 4g,h), which agrees with our EDS results on the multilayer MXenes (Table S1). Several important conclusions can be drawn from the XPS depth profiling. Quantitatively, the distribution of Ti, V, Nb/Cr, Mo, and C was relatively constant through the MXene

https://doi.org/10.1021/acsnano.1c02775
ACS Nano XXXX, XXX, XXX–XXX

films, suggesting that the MXenes have a relatively uniform distribution of the transition metals in the structure. With increasing depth, the concentration of each transition metal element approaches the equimolar concentration of the high-entropy MXenes as observed in their precursor MAX phases. This also indicates that the topochemical etching process in aqueous HF and the delamination process did not alter the transition metal ratios.

To further characterize the composition of the synthesized high-entropy MXenes, scanning transmission electron microscopy (STEM) analysis combined with EDS was performed to better understand the elemental distribution and nanostructure of $TiVNbMoC_3T_x$ and $TiVCrMoC_3T_x$ flakes to confirm their four-atomic-layer structure and map their elements. To accurately probe the structure of these MXenes, both samples were drop-cast from delaminated MXene solutions on a lacey-carbon-coated Cu grid (see Methods Section for more details). Figure 4i shows a high-angle annular dark-field (HAADF) STEM image of $TiVNbMoC_3T_x$, indicating that each MXene flake is composed of four transition metal atomic layers, in agreement with previously reported STEM of $M_4C_3T_x$ MXenes.[12,48] EDS mapping (Figures 4j and S6) of each MXene compositions reveals that Ti, V, Nb/Cr, Mo, and C are distributed across the transition metal layers, signifying the near equimolar distribution of the transition metals in high-entropy MXenes.

Next, we carried out computational studies based on first-principles approaches. To understand the synthesizability of high-entropy MAX and MXene phases as well as to quantify the thermodynamic stability of the MAX compositions, we investigated the formation enthalpy (ΔH) of the MAX compositions with reference to the combination of most competitive phases, $\Delta H_{cp} = \Delta H_{MAX\ phase} - \Delta H_{competitive\ phases}$. The formation enthalpy of different phases was calculated using the total energy of those phase structures and the total energies (per atom) of the M, A, and X elements in their standard state (bulk phases). The most competing phases were then identified using a linear optimization process.[68] The negative ΔH_{cp} specifies the relative stability of MAX phases with respect to the competitive phases. In general, the more negative the enthalpy values indicates the higher possibility for their experimental realization. The compositions of the MAX phases along with their enthalpies of formation as well as lattice parameters are given in Table S4. The Bader charges of the transition metals for both high-entropy MAX phases are also presented in Table S5. The calculated electron concentration of the already synthesized MAX phases with reference to their relative formation energies is shown in Figure S7.

In multicomponent systems, a major contributor to their stabilization arises from configurational entropy, *i.e.*, statistically the number of discrete representative positions of the alloy constituents, which is dependent on the number of elements in the system under consideration. The entropic contribution for the three-transition-metal (three-M) and four-transition-metal (four-M) MAX systems can be calculated using[69]

$$\Delta S_{mix} = -R \sum_{i=1}^{k} x_i \ln x_i$$

where x_i is the mole fraction of the ith component in a system with k total components.[22] The calculated entropic contribution at 1600 °C for three-M and four-M systems are −0.1773 and −0.2238 eV/f.u., respectively. Based on configurational entropy, the four-M MAX phase has more favorable entropy to form as a single phase compared to the three-M one (Figure S8). The entropic stabilization explains the preference for the four-M single-phase MAX phase as compared to three-M phases of MAX under similar synthesis conditions. Note, however, that our enthalpy calculations reveal that the three-M MAX is also synthesizable (Table S4). Since we only used one synthesis temperature and duration (1600 °C, 4 h) for the sake of consistency, we cannot rule out the single-phase formation of the three-M MAX by further annealing at a desired temperature and duration. It is known that a lower contribution of configurational entropy can lead to the formation of a multiphase system (undesired phases) in the absence of postannealing treatment.[25] Further detailed studies on the nature of competing phases and formation pathways are required to understand the trends in synthesizability of high-entropy MAX phases.

CONCLUSIONS AND FUTURE OUTLOOK

In summary, we have synthesized the two high-entropy $TiVNbMoAlC_3$ and $TiVCrMoAlC_3$ MAX phases and turn them to high-entropy $TiVNbMoC_3T_x$ and $TiVCrMoC_3T_x$ MXenes with an equimolar proportion of Ti:V:Nb:Mo and Ti:V:Cr:Mo principal transition metals. We formed these high-entropy MAX phases using traditional pressureless reactive sintering and synthesized their respective single-to-few-layer MXenes utilizing hydrofluoric acid-based selective etching followed by tetramethylammonium hydroxide delamination. We confirmed the synthesis and purity of our high-entropy MAX phases and their successful synthesis to single-to-few-layer high-entropy MXenes using XRD, SEM, and STEM. In addition, we confirmed the bonding characteristics in high-entropy MXenes using XPS and identified the equimolar composition of transition metals utilizing EDS in SEM. We further establish the equimolar distribution of transition metals in the transition metal layers in the delaminated single-to-few-layer MXenes using elemental mapping with EDS in STEM. Our first-principles calculations trace the synthesizability of quaternary high-entropy MAX to an entropy-driven stabilization and highlight the importance of high configurational entropy in equimolar multielements in forming pure and stable phases of MPE MAX phases. We thus report on the successful synthesis of high-entropy MAX and MXene materials by maximizing the configurational entropy to stabilize (near) equimolar mixtures in a fashion analogous to that in other disordered multicomponent systems (*e.g.*, bulk ceramics and metals). Successful synthesis of this exotic subgroup of high-entropy MPE MXenes adds a large possible compositional space to the growing family of MXenes, which can be explored for applications including energy storage, catalysis, and microstructural stability in extreme environments.

We have laid the groundwork for further studies to focus on a comprehensive analysis of more compositions of high-entropy MAX phases and their derived MXenes to further analyze stable compositions using both computational and experimental methods. Furthermore, an understanding of the control of the composition of each transition metal layer of MXenes could also play a significant role in future tailoring of their electrochemical, catalytic, electrical, and magnetic properties. A certain selection of multiple constituent transition metals can further enable the development of

https://doi.org/10.1021/acsnano.1c02775
ACS Nano XXXX, XXX, XXX−XXX

topological insulator MXenes, which have not been synthesized yet but are predicted in theoretical studies,[70,71] specifically due to larger degrees of freedom in component selectivity and phase formation using more than one transition metal in MXenes.

From a computational perspective, the enormous compositional space coupled with the possibility of entropic stabilization in high-entropy MAX and MXene phases creates many different directions as well as challenges. Traditional modeling approaches can be combined with recent advances in big data analytics to answer several intriguing questions related to quantitative calculation of the entropy, prediction of thermochemical properties, the transition temperatures, and investigation of their transport properties to better understand the mechanisms affecting their synthesizability. We envision many opportunities for Monte Carlo simulations in computing entropic contributions; this would require many energetic contributions that would benefit from cluster expansion and other machine learning methods that build surrogate models based on *ab-initio* training data. The kinetic aspects could be probed with molecular dynamics that can shed light on the diffusion rates in disordered materials. Recent data-driven approaches can also provide useful information on the lifetimes and stability of metastable phases under different operating conditions. Overall, the vast quantity of synthetic and experimental data sets that will be generated creates tremendous opportunities for artificial intelligence and machine learning to identify critical trends for accelerating materials design and materials discovery in this important class of high-entropy 2D materials.

METHODS SECTION

Synthesis of High-Entropy MAX Phases. All elements Ti (325 mesh), V (325 mesh), Mo (250 mesh), Nb (325 mesh), Cr (325 mesh), Al(325 mesh), and C (calcinated coke, 325 mesh) and reagents HF (48 wt % aqueous) and TMAOH (25% w/w aqueous) were obtained from Fisher Scientific and used without further processing unless specified.

For Al and C, we followed the typical ratios that we always use for the synthesis of M_4AlC_3.[48,58] In general, we add an additional amount (~0.1 mol) of Al to compensate for any evaporation during the MAX synthesis.[49,72] In general, the Al to transition metal ratio in MAX phases of similar structures (M_4AC_3 here) is similar regardless of the transition metal type. We also use less than a stoichiometric ratio of C, as we know MAX phases are usually carbon deficient, similar to binary transition metal carbides.[49,73]

Molar ratios of the elemental powders for Ti:V:Nb:Mo:Al:C and Ti:V:Cr:Mo:Al:C were 1:1:1:1:1.1:2.7, respectively, and the blends were milled in polyethylene jars on a tumbler mill with zirconia balls at a powder to ball weight ratio of 1:5 for 18 h at 60 rpm. Ball-milled powders were transferred to alumina crucibles and sintered in a conventional tube furnace (Carbolite Gero) fitted with an alumina tube at 1600 °C, held for 4 h. The temperature ramp rate was 3.5 °C/min. The furnace was flushed with Ar gas for 10−15 min prior to firing of the MAX powders. A constant Ar flow was maintained throughout the run until the samples reached room temperature. After cooling, the synthesized MAX phases were drilled with a TiN-coated drill bit and sieved with a 40 μm sieve to obtain uniform grains of MAX powder for etching.

Synthesis and Delamination of High-Entropy MXenes. MXenes (both $TiVNbMoC_3$ and $TiVCrMoC_3$) were synthesized *via* top-down synthesis, by selective etching of their respective MAX phases. In a typical experiment, 2 g of MAX was added slowly (~60 s) to a polyethylene jar filled with 20 mL of HF (48 wt %) and held at 55 °C with continuous stirring at 400 rpm for 4 days. The etched MXene was washed repeatedly four or five times (~250 mL with DI water) in a centrifuge at 4200 rpm with each typical run lasting 3−5 min. The pH (>6) neutralized etched MXene cakes were obtained *via* vacuum-assisted filtration with a 2.5 μm cellulose filter paper. The etching process is identical for both $TiVNbMoAlC_3$ and $TiVCrMoAlC_3$ phases.

Filtered MXene cakes were subsequently delaminated with 5 wt % TMAOH with continuous stirring at 500−600 rpm for 4 h at 55 °C. The delaminated MXenes were washed repeatedly five times (~250 mL with DI water) in a centrifuge at 10 000 rpm with variable times (5−10 min) to bring the pH to ~6. The supernatant was collected, and films were made by vacuum-assisted filtration. Figure S3 shows the supernatant, clay, and films of $TiVCrMoC_3$ and $TiVNbMoC_3$ MXenes.

Microstructural Characterization. *XRD.* The structural characteristics of the MAX phases and MXenes were obtained using a Bruker D8 Discover X-ray diffractometer with a Cu K(alpha) radiation wavelength of 1.541 84 Å paired with the Vantec two-dimensional detector (XRD^2). The scans were carried out from 5−75 deg 2θ (0−90°) using step sizes of 5° 2θ with a time step of 60 s/step. MAX phase and multilayer MXene powders were placed into cylindrical holes on an aluminum substrate with dimensions 5 mm diameter × 1.5 mm depth. The MAX powders were preferentially ordered using a clean glass slide for pressing on the top of the powder samples. $TiVNbMoC_3$ and $TiVCrMoC_3$ MXene single-to-few-layer films were cut into 5 mm × 10 mm rectangular pieces, and one of these film pieces was stacked on an amorphous double-sided carbon tape on a clean glass substrate. The sample height was aligned using dual-focused laser beams. Spectral data were analyzed with crystal impact software, Match!

SEM/EDS. A JEOL JSM-7800F FESEM equipped with an in-lens thermal field emission electron gun and a conical objective lens with in-tandem upper and lower electron detectors was used to collect morphological and compositional data of the samples. All specimens were sputter-coated with gold (Denton Desk V Turbo) to enhance conduction on the surface. Energy dispersion spectroscopy was performed *via* an EDAX Octane Super Detector and associated EDAX TEAM software. The working distance (10 mm) and elevation angle (35°) were fixed along with a scale setting of 58 for the EDS analyses. The dead time for each run was manually adjusted to 27−35. A random spot was selected and was analyzed pointwise (at 10 spots) with an excitation voltage of 15−25 kV and a peak current of 8−10 amp. A magnification of 1000k× was used for obtaining the composition of the MXene films.

XPS and STEM/EDS. X-ray photoelectron spectroscopy spectra were collected for each MXene using the free-standing films, made by vacuum filtration of their delaminated solutions, on a Thermo K-alpha XPS system with a spot size of 400 μm at an energy resolution of 0.1 eV. Ar^+ sputtering was carried out with a beam energy of 4 eV, and the cluster size was 1000 atoms. For the XPS depth profiles, the atomic percentages were calculated for only Ti, V, Mo, Cr/Nb, and C. All XPS spectra were analyzed using Thermo Avantage, a software package provided through ThermoScientific. Scanning transmission electron microscopy was performed on an FEI Talos TEM/STEM equipped with an EDS detector (Bruker) operated at 200 kV. Elemental maps were collected with a STEM spot size of 6. All S/TEM specimens were prepared by dispersing freestanding MXene films, made from delaminated MXene solutions, in DI H_2O, and drop-casting the dispersion onto lacey-carbon-coated copper grids.

First-Principles Calculations. To simulate the chemical disorder of actual high-entropy MAX while maintaining a tractable size for the computational cell, we used special quasi-random structures (SQSs) using the ATAT software package.[74] For the four-transition-metal MAX phase, we utilized a 2 × 2 × 1 supercell, whereas in the case of the three-transition-metal system, a supercell of 3 × 3 × 1 from the parent MAX phase was used. The Perdue−Burke−Ernzerhof (PBE)[75] exchange−correlation functional and the projected augmented wave approach[45,46] were used through its implementation in the Vienna *ab-Initio* Simulation Package (VASP).[76−78] The MAX phase structures were fully optimized through relaxation of the unit-cell shape, atomic positions, and volume using the conjugate gradient method until the

https://doi.org/10.1021/acsnano.1c02775
ACS Nano XXXX, XXX, XXX−XXX

maximum residual force acting on each atom became less than 0.01 eV/Å. The electronic energy convergence criterion used is 10^{-6} eV/cell, having a plane wave cutoff energy of 520 eV. The Brillouin zone was integrated using the Monkhorst−Pack *k*-point sampling method.[79] A dense *k*-point grid was employed, defined by $n_{atoms} \times n_{k\text{-points}} \approx 1000$, where n_{atoms} is the number of atoms in the primitive cell and $n_{k\text{-points}}$ is the number of *k*-points, respectively.[80]

ASSOCIATED CONTENT

Supporting Information

The Supporting Information is available free of charge at https://pubs.acs.org/doi/10.1021/acsnano.1c02775.

Differential scanning calorimetry plots for the high-entropy MAX powder mixtures, tables of EDS analysis of high-entropy MAX phases and MXenes in SEM, XRD patterns of different ratios of Ti:V:Nb:Mo:Al:C, Ti:V:Nb:Mo:Al:C, and Ti:V:Cr:Mo:Al:C, digital photos of different stages of $TiVCrMoC_3T_x$ and $TiVNbMoC_3T_x$ synthesis, SEM images of $TiVNbMoC_3T_x$ and $TiVCrMoC_3T_x$ MXene films, XPS spectra of $TiVNbMoC_3T_x$ and $TiVCrMoC_3T_x$ showing the surface functional groups −O and −F, HAADF STEM images of $TiVNbMoC_3T_x$ and $TiVCrMoC_3T_x$ flakes, EDS map of $TiVCrMoC_3T_x$ flakes, XPS deconvolution data with binding energy for $TiVNbMoC_3T_x$ and $TiVCrMoC_3T_x$, calculated enthalpy of formation of $TiVCrMoAlC_3$, $TiVNbMoAlC_3$, and $(Ti_{1.33}V_{1.33}Nb_{1.33})AlC_3$ MAX phases, Bader charges of transition metal elements in the high-entropy MAX phases, calculated electron concentration of the already synthesized MAX phases with reference to their relative formation energy, configurational entropy of two-M, three-M, and four-M phases as a function of the last constituent mol % (PDF)

AUTHOR INFORMATION

Corresponding Authors

Subramanian K. R. S. Sankaranarayanan − *Center for Nanoscale Materials, Argonne National Laboratory, Lemont, Illinois 60439, United States; Department of Mechanical and Industrial Engineering, University of Illinois, Chicago, Illinois 60607, United States*; Email: skrssank@uic.edu

Babak Anasori − *Department of Mechanical and Energy Engineering, Purdue School of Engineering and Technology and Integrated Nanosystems Development Institute, Indiana University-Purdue University Indianapolis, Indianapolis, Indiana 46202, United States*; orcid.org/0000-0002-1955-253X; Email: banasori@iupui.edu

Authors

Srinivasa Kartik Nemani − *Department of Mechanical and Energy Engineering, Purdue School of Engineering and Technology and Integrated Nanosystems Development Institute, Indiana University-Purdue University Indianapolis, Indianapolis, Indiana 46202, United States*

[¶]Bowen Zhang − *Department of Mechanical and Energy Engineering, Purdue School of Engineering and Technology and Integrated Nanosystems Development Institute, Indiana University-Purdue University Indianapolis, Indianapolis, Indiana 46202, United States*

Brian C. Wyatt − *Department of Mechanical and Energy Engineering, Purdue School of Engineering and Technology and Integrated Nanosystems Development Institute, Indiana University-Purdue University Indianapolis, Indianapolis, Indiana 46202, United States*

Zachary D. Hood − *Applied Materials Division, Argonne National Laboratory, Lemont, Illinois 60439, United States*

Sukriti Manna − *Center for Nanoscale Materials, Argonne National Laboratory, Lemont, Illinois 60439, United States; Department of Mechanical and Industrial Engineering, University of Illinois, Chicago, Illinois 60607, United States*

Rasoul Khaledialidusti − *Department of Mechanical and Industrial Engineering, Norwegian University of Science and Technology (NTNU), 7491 Trondheim, Norway*

Weichen Hong − *Department of Mechanical and Energy Engineering, Purdue School of Engineering and Technology, Indiana University-Purdue University Indianapolis, Indianapolis, Indiana 46202, United States*

Michael G. Sternberg − *Center for Nanoscale Materials, Argonne National Laboratory, Lemont, Illinois 60439, United States*

Complete contact information is available at: https://pubs.acs.org/10.1021/acsnano.1c02775

Notes

The authors declare no competing financial interest.

[¶]Permanent Address: (B.Z.) Henan Key Laboratory of Photovoltaic Materials, Henan University, Kaifeng 475004, People's Republic of China.

This manuscript was previously submitted to the preprint server ChemRxiv on March 31, 2021. The preprint version can be found under the following: S. K. Nemani, B. Zhang, B. C. Wyatt, Z. D. Hood, S. Manna, R. Khaledialidusti, W. Hong, M. G. Sternberg, S. Sankaranarayanan, B. Anasori. High-Entropy 2D Carbide MXenes. 2021. ChemRxiv, Preprint. 10.26434/chemrxiv.14346953.v1 (April 1, 2021).

ACKNOWLEDGMENTS

B.A. acknowledge startup funding from the Department of Mechanical and Energy Engineering and Purdue School of Engineering and Technology at IUPUI. Z.D.H. was supported by Laboratory Directed Research and Development (LDRD) funding from Argonne National Laboratory, provided by the Director, Office of Science, of the U.S. Department of Energy under Contract No. DE-AC02-06CH11357. The computational material is based upon work supported by the U.S. Department of Energy, Office of Science, Office of Basic Energy Sciences Data, Artificial Intelligence and Machine Learning at DOE Scientific User Facilities program under Award Number 34532. Use of the Center for Nanoscale Materials, an Office of Science user facility, was supported by the U.S. Department of Energy, Office of Science, Office of Basic Energy Sciences, under Contract No. DE-AC02-06CH11357. This research used resources of the National Energy Research Scientific Computing Center, which was supported by the Office of Science of the U.S. Department of Energy under Contract No. DE-AC02-05CH11231. An award of computer time was provided by the Innovative and Novel Computational Impact on Theory and Experiment (INCITE) program of the Argonne Leadership Computing Facility at the Argonne National Laboratory, which was supported by the Office of Science of the U.S. Department of Energy under Contract No. DE-AC02-06CH11357. S.K.R.S.S. acknowledges UIC start-up funds for supporting this research. B.Z. acknowledges the support from Henan Key Laboratory of

Photovoltaic Materials, Henan University, Kaifeng, China. The authors thank the National Science Foundation Major Research Instrumentation Program for support (Award 1229514 for FESEM and Award 1429241 for XRD). Any opinions, findings, and conclusions or recommendations expressed in this material are those of the author(s) and do not necessarily reflect the views of the National Science Foundation.

REFERENCES

(1) Naguib, M.; Mashtalir, O.; Carle, J.; Presser, V.; Lu, J.; Hultman, L.; Gogotsi, Y.; Barsoum, M. W. Two-Dimensional Transition Metal Carbides. *ACS Nano* **2012**, *6* (2), 1322−1331.

(2) Naguib, M.; Kurtoglu, M.; Presser, V.; Lu, J.; Niu, J.; Heon, M.; Hultman, L.; Gogotsi, Y.; Barsoum, M. W. Two-Dimensional Nanocrystals Produced by Exfoliation of Ti_3AlC_2. *Adv. Mater.* **2011**, *23* (37), 4248−4253.

(3) Anasori, B.; Lukatskaya, M. R.; Gogotsi, Y. 2D Metal Carbides and Nitrides (MXenes) for Energy Storage. *Nature Reviews Materials* **2017**, *2* (2), 16098.

(4) Deysher, G.; Shuck, C. E.; Hantanasirisakul, K.; Frey, N. C.; Foucher, A. C.; Maleski, K.; Sarycheva, A.; Shenoy, V. B.; Stach, E. A.; Anasori, B. Synthesis of Mo_4VAlC_4 MAX Phase and Two-Dimensional Mo_4VC_4 MXene with 5 Atomic Layers of Transition Metals. *ACS Nano* **2020**, *14*, 204−217.

(5) Wang, H.-W.; Naguib, M.; Page, K.; Wesolowski, D. J.; Gogotsi, Y. Resolving the Structure of $Ti_3C_2T_x$ MXenes Through Multi-Level Structural Modeling of the Atomic Pair Distribution Function. *Chem. Mater.* **2016**, *28* (1), 349−359.

(6) Gogotsi, Y.; Anasori, B. The Rise of MXenes. *ACS Nano* **2019**, *13* (8), 8491−8494.

(7) Khaledialidusti, R.; Khazaei, M.; Khazaei, S.; Ohno, K. High-Throughput Computational Discovery of Ternary-Layered MAX Phases and Prediction of Their Exfoliation for Formation of 2D MXenes. *Nanoscale* **2021**, *13*, 7294−7307.

(8) Mathis, T.; Maleski, K.; Goad, A.; Sarycheva, A.; Anayee, M.; Foucher, A. C.; Hantanasirisakul, K.; Stach, E.; Gogotsi, Y.; Alexandre, C. Modified MAX Phase Synthesis for Environmentally Stable and Highly Conductive Ti_3C_2 MXene. *ACS Nano* **2021**, *15* (4), 6420−6429.

(9) Lipatov, A.; Alhabeb, M.; Lu, H.; Zhao, S.; Loes, M. J.; Vorobeva, N. S.; Dall'Agnese, Y.; Gao, Y.; Gruverman, A.; Gogotsi, Y.; Sinitskii, A. Electrical and Elastic Properties of Individual Single-Layer $Nb_4C_3T_x$ MXene Flakes. *Advanced Electronic Materials* **2020**, *6* (4), 1901382.

(10) Lim, K. R. G.; Handoko, A. D.; Nemani, S. K.; Wyatt, B.; Jiang, H.-Y.; Tang, J.; Anasori, B.; Seh, Z. W. Rational Design of Two-Dimensional Transition Metal Carbide/Nitride (MXene) Hybrids and Nanocomposites for Catalytic Energy Storage and Conversion. *ACS Nano* **2020**, *14* (9), 10834−10864.

(11) Verger, L.; Xu, C.; Natu, V.; Cheng, H.-M.; Ren, W.; Barsoum, M. W. Overview of the Synthesis of MXenes and Other Ultrathin 2D Transition Metal Carbides and Nitrides. *Curr. Opin. Solid State Mater. Sci.* **2019**, *23* (3), 149−163.

(12) Anasori, B.; Xie, Y.; Beidaghi, M.; Lu, J.; Hosler, B. C.; Hultman, L.; Kent, P. R. C.; Gogotsi, Y.; Barsoum, M. W. Two-Dimensional, Ordered, Double Transition Metals Carbides (MXenes). *ACS Nano* **2015**, *9* (10), 9507−9516.

(13) Tao, Q.; Dahlqvist, M.; Lu, J.; Kota, S.; Meshkian, R.; Halim, J.; Palisaitis, J.; Hultman, L.; Barsoum, M. W.; Persson, P. O.; Rosen, J. Two-Dimensional $Mo_{1.33}C$ MXene with Divacancy Ordering Prepared from Parent 3D Laminate with In-Plane Chemical Ordering. *Nat. Commun.* **2017**, *8* (1), 14949.

(14) Maleski, K.; Shuck, C. E.; Fafarman, A. T.; Gogotsi, Y. The Broad Chromatic Range of Two-Dimensional Transition Metal Carbides. *Adv. Opt. Mater.* **2021**, *9* (4), 2001563.

(15) Han, M.; Shuck, C. E.; Rakhmanov, R.; Parchment, D.; Anasori, B.; Koo, C. M.; Friedman, G.; Gogotsi, Y. Beyond $Ti_3C_2T_x$: MXenes for Electromagnetic Interference Shielding. *ACS Nano* **2020**, *14* (4), 5008−5016.

(16) Hong, W.; Wyatt, B. C.; Nemani, S. K.; Anasori, B. Double Transition-Metal MXenes: Atomistic Design of Two-Dimensional Carbides and Nitrides. *MRS Bull.* **2020**, *45* (10), 850−861.

(17) Han, M.; Maleski, K.; Shuck, C. E.; Yang, Y.; Glazar, J. T.; Foucher, A. C.; Hantanasirisakul, K.; Sarycheva, A.; Frey, N. C.; May, S. J.; Shenoy, V. B.; Stach, E. A.; Gogotsi, Y. Tailoring Electronic and Optical Properties of MXenes through Forming Solid Solutions. *J. Am. Chem. Soc.* **2020**, *142* (45), 19110−19118.

(18) Hantanasirisakul, K.; Anasori, B.; Nemsak, S.; Hart, J. L.; Wu, J.; Yang, Y.; Chopdekar, R. V.; Shafer, P.; May, A. F.; Moon, E. J.; Zhou, J.; Zhang, Q.; Taheri, M. L.; May, S. J.; Gogotsi, Y. Evidence of a Magnetic Transition in Atomically Thin $Cr_2TiC_2T_x$ MXene. *Nanoscale Horizons* **2020**, *5* (12), 1557−1565.

(19) Khazaei, M.; Ranjbar, A.; Arai, M.; Yunoki, S. Topological Insulators in Ordered Double Transition Metals $M'_2M''C_2$ (M'= Mo, W; M''= Ti, Zr, Hf) MXenes. *Phys. Rev. B: Condens. Matter Mater. Phys.* **2016**, *94* (12), 125−152.

(20) Yeh, J. W.; Chen, S. K.; Lin, S. J.; Gan, J. Y.; Chin, T. S.; Shun, T. T.; Tsau, C. H.; Chang, S. Y. Nanostructured High-Entropy Alloys with Multiple Principal Elements: Novel Alloy Design Concepts and Outcomes. *Adv. Eng. Mater.* **2004**, *6* (5), 299−303.

(21) Cantor, B.; Chang, I. T. H.; Knight, P.; Vincent, A. J. B. Microstructural Development in Equiatomic Multicomponent Alloys. *Mater. Sci. Eng., A* **2004**, *375*−*377*, 213−218.

(22) Ye, Y. F.; Wang, Q.; Lu, J.; Liu, C. T.; Yang, Y. High-Entropy Alloy: Challenges and Prospects. *Mater. Today* **2016**, *19* (6), 349−362.

(23) Koo, W.-T.; Millstone, J. E.; Weiss, P. S.; Kim, I.-D. The Design and Science of Polyelemental Nanoparticles. *ACS Nano* **2020**, *14* (6), 6407−6413.

(24) George, E. P.; Raabe, D.; Ritchie, R. O. High-Entropy Alloys. *Nature Reviews Materials* **2019**, *4* (8), 515−534.

(25) Oses, C.; Toher, C.; Curtarolo, S. High-Entropy Ceramics. *Nature Reviews Materials* **2020**, *5* (4), 295−309.

(26) Rost, C. M.; Sachet, E.; Borman, T.; Moballegh, A.; Dickey, E. C.; Hou, D.; Jones, J. L.; Curtarolo, S.; Maria, J.-P. Entropy-Stabilized Oxides. *Nat. Commun.* **2015**, *6* (1), 1−8.

(27) Zhou, J.; Zhang, J.; Zhang, F.; Niu, B.; Lei, L.; Wang, W. High-Entropy Carbide: A Novel Class of Multicomponent Ceramics. *Ceram. Int.* **2018**, *44* (17), 22014−22018.

(28) Wang, F.; Yan, X.; Wang, T.; Wu, Y.; Shao, L.; Nastasi, M.; Lu, Y.; Cui, B. Irradiation Damage in $(Zr_{0.25}Ta_{0.25}Nb_{0.25}Ti_{0.25})C$ High-Entropy Carbide Ceramics. *Acta Mater.* **2020**, *195*, 739−749.

(29) Gild, J.; Zhang, Y.; Harrington, T.; Jiang, S.; Hu, T.; Quinn, M. C.; Mellor, W. M.; Zhou, N.; Vecchio, K.; Luo, J. High-Entropy Metal Diborides: A New Class of High-Entropy Materials and a New Type of Ultrahigh Temperature Ceramics. *Sci. Rep.* **2016**, *6* (1), 37946.

(30) Castle, E.; Csanádi, T.; Grasso, S.; Dusza, J.; Reece, M. Processing and Properties of High-Entropy Ultra-High Temperature Carbides. *Sci. Rep.* **2018**, *8* (1), 1−12.

(31) Sarker, P.; Harrington, T.; Toher, C.; Oses, C.; Samiee, M.; Maria, J.-P.; Brenner, D. W.; Vecchio, K. S.; Curtarolo, S. High-Entropy High-Hardness Metal Carbides Discovered by Entropy Descriptors. *Nat. Commun.* **2018**, *9* (1), 4980.

(32) Feng, L.; Chen, W.-T.; Fahrenholtz, W. G.; Hilmas, G. E. Strength of Single-Phase High-Entropy Carbide Ceramics up to 2300°C. *J. Am. Ceram. Soc.* **2021**, *104* (1), 419−427.

(33) Wang, K.; Chen, L.; Xu, C.; Zhang, W.; Liu, Z.; Wang, Y.; Ouyang, J.; Zhang, X.; Fu, Y.; Zhou, Y. Microstructure and Mechanical Properties of (TiZrNbTaMo) C High-Entropy Ceramic. *J. Mater. Sci. Technol.* **2020**, *39*, 99−105.

(34) Liu, D.; Zhang, A.; Jia, J.; Meng, J.; Su, B. Phase Evolution and Properties of (VNbTaMoW) C High Entropy Carbide Prepared by Reaction Synthesis. *J. Eur. Ceram. Soc.* **2020**, *40* (8), 2746−2751.

(35) Gild, J.; Kaufmann, K.; Vecchio, K.; Luo, J. Reactive Flash Spark Plasma Sintering of High-Entropy Ultrahigh Temperature Ceramics. *Scr. Mater.* **2019**, *170*, 106−110.

https://doi.org/10.1021/acsnano.1c02775
ACS Nano XXXX, XXX, XXX−XXX

(36) Ye, B.; Wen, T.; Huang, K.; Wang, C.-Z.; Chu, Y. First-Principles Study, Fabrication, and Characterization of $(Hf_{0.2}Zr_{0.2}Ta_{0.2}Nb_{0.2}Ti_{0.2})C$ High-Entropy Ceramic. *J. Am. Ceram. Soc.* **2019**, *102* (7), 4344−4352.
(37) Wei, X.-F.; Liu, J.-X.; Li, F.; Qin, Y.; Liang, Y.-C.; Zhang, G.-J. High Entropy Carbide Ceramics from Different Starting Materials. *J. Eur. Ceram. Soc.* **2019**, *39* (10), 2989−2994.
(38) Ye, B.; Wen, T.; Liu, D.; Chu, Y. Oxidation Behavior of $(Hf_{0.2}Zr_{0.2}Ta_{0.2}Nb_{0.2}Ti_{0.2})C$ High-Entropy Ceramics at 1073−1473 K in Air. *Corros. Sci.* **2019**, *153*, 327−332.
(39) Tan, Y.; Chen, C.; Li, S.; Han, X.; Xue, J.; Liu, T.; Zhou, X.; Zhang, H. Oxidation Behaviours of High-Entropy Transition Metal Carbides in 1200 °C Water Vapor. *J. Alloys Compd.* **2020**, *816*, 152523.
(40) Vladescu, A.; Titorencu, I.; Dekhtyar, Y.; Jinga, V.; Pruna, V.; Balaceanu, M.; Dinu, M.; Pana, I.; Vendina, V.; Braic, M. *In Vitro* Biocompatibility of Si Alloyed Multi-Principal Element Carbide Coatings. *PLoS One* **2016**, *11* (8), No. e0161151.
(41) Andreyev, A.; Kartmazov, G.; Chikryzhov, A.; Karpets, M.; Dolomanov, A.; Ostroverkh, A.; Kantsyr, E. Production and Mechanical Properties of High-Entropic Carbide Based on the TiZrHfVNbTa Multicomponent Alloy. *Journal of Superhard Materials* **2017**, *39* (3), 166−171.
(42) Braic, V.; Balaceanu, M.; Braic, M.; Vladescu, A.; Panseri, S.; Russo, A. Characterization of Multi-Principal-Element (TiZrNbHfTa)N and (TiZrNbHfTa)C Coatings for Biomedical Applications. *Journal of the Mechanical Behavior of Biomedical Materials* **2012**, *10*, 197−205.
(43) Hlova, I. Z.; Dolotko, O.; Boote, B. W.; Pathak, A. K.; Smith, E. A.; Pecharsky, V. K.; Balema, V. P. Multi-Principal Element Transition Metal Dichalcogenides *via* Reactive Fusion of 3D-Heterostructures. *Chem. Commun.* **2018**, *54* (89), 12574−12577.
(44) Lan, T.; H, I.; Pecharsky, V.; Pathak, A.; Balema, V.; Padalkar, S. High-Entropy Transition Metal Dichalcogenides as Exceptional Electrocatalysts of Hydrogen Evolution Reaction (HER). *ECS Meeting Abstracts* **2019**, *41*, 1964.
(45) Blöchl, P. E. Projector Augmented-Wave Method. *Phys. Rev. B: Condens. Matter Mater. Phys.* **1994**, *50* (24), 17953−17979.
(46) Kresse, G.; Joubert, D. From Ultrasoft Pseudopotentials to the Projector Augmented-Wave Method. *Phys. Rev. B: Condens. Matter Mater. Phys.* **1999**, *59* (3), 1758−1775.
(47) Dahlqvist, M.; Rosen, J. Predictive Theoretical Screening of Phase Stability for Chemical Order and Disorder in Quaternary 312 and 413 MAX Phases. *Nanoscale* **2020**, *12* (2), 785−794.
(48) Pinto, D.; Anasori, B.; Avireddy, H.; Shuck, C. E.; Hantanasirisakul, K.; Deysher, G.; Morante, J. R.; Porzio, W.; Alshareef, H. N.; Gogotsi, Y. Synthesis and Electrochemical Properties of 2D Molybdenum Vanadium Carbides−Solid Solution MXenes. *J. Mater. Chem. A* **2020**, *8* (18), 8957−8968.
(49) Sokol, M.; Natu, V.; Kota, S.; Barsoum, M. W. On the Chemical Diversity of the MAX Phases. *Trends in Chemistry* **2019**, *1* (2), 210−223.
(50) Naguib, M.; Bentzel, G. W.; Shah, J.; Halim, J.; Caspi, E. N.; Lu, J.; Hultman, L.; Barsoum, M. W. New Solid Solution MAX Phases: $(Ti_{0.5}, V_{0.5})_3AlC_2$, $(Nb_{0.5}, V_{0.5})_2AlC$, $(Nb_{0.5}, V_{0.5})_4AlC_3$ and $(Nb_{0.8}, Zr_{0.2})_2AlC$. *Mater. Res. Lett.* **2014**, *2* (4), 233−240.
(51) Yang, J.; Naguib, M.; Ghidiu, M.; Pan, L. M.; Gu, J.; Nanda, J.; Halim, J.; Gogotsi, Y.; Barsoum, M. W. Two-Dimensional Nb-Based M_4C_3 Solid Solutions (MXenes). *J. Am. Ceram. Soc.* **2016**, *99* (2), 660−666.
(52) Alhabeb, M.; Maleski, K.; Anasori, B.; Lelyukh, P.; Clark, L.; Sin, S.; Gogotsi, Y. Guidelines for Synthesis and Processing of 2D Titanium Carbide ($Ti_3C_2T_x$ MXene). *Chem. Mater.* **2017**, *29* (18), 7633−7644.
(53) Anasori, B.; Shi, C.; Moon, E. J.; Xie, Y.; Voigt, C. A.; Kent, P. R. C.; May, S. J.; Billinge, S. J. L.; Barsoum, M. W.; Gogotsi, Y. Control of Electronic Properties of 2D Carbides (MXenes) by Manipulating Their Transition Metal Layers. *Nanoscale Horizons* **2016**, *1* (3), 227−234.
(54) Hantanasirisakul, K.; Alhabeb, M.; Lipatov, A.; Maleski, K.; Anasori, B.; Salles, P.; Ieosakulrat, C.; Pakawatpanurut, P.; Sinitskii, A.; May, S. J.; Gogotsi, Y. Effects of Synthesis and Processing on Optoelectronic Properties of Titanium Carbonitride MXene. *Chem. Mater.* **2019**, *31*, 2941−2951.
(55) Fredrickson, K. D.; Anasori, B.; Seh, Z. W.; Gogotsi, Y.; Vojvodic, A. Effects of Applied Potential and Water Intercalation on the Surface Chemistry of Ti_2C and Mo_2C MXenes. *J. Phys. Chem. C* **2016**, *120* (50), 28432−28440.
(56) Wyatt, B. C.; Rosenkranz, A.; Anasori, B. 2D MXenes: Tunable Mechanical and Tribological Properties. *Adv. Mater.* **2021**, *33* (17), 2007973.
(57) Shekhirev, M.; Shuck, C. E.; Sarycheva, A.; Gogotsi, Y. Characterization of MXenes at Every Step, from Their Precursors to Single Flakes and Assembled Films. *Prog. Mater. Sci.* **2020**, 100757.
(58) Anasori, B.; Dahlqvist, M.; Halim, J.; Moon, E. J.; Lu, J.; Hosler, B. C.; El'ad, N. C.; May, S. J.; Hultman, L.; Eklund, P.; Rosen, J.; Barsoum, M. W. Experimental and Theoretical Characterization of Ordered MAX Phases Mo_2TiAlC_2 and $Mo_2Ti_2AlC_3$. *J. Appl. Phys.* **2015**, *118* (9), No. 094304.
(59) Anasori, B.; Halim, J.; Lu, J.; Voigt, C. A.; Hultman, L.; Barsoum, M. W. Mo_2TiAlC_2: A New Ordered Layered Ternary Carbide. *Scr. Mater.* **2015**, *101*, 5−7.
(60) Meshkian, R.; Tao, Q.; Dahlqvist, M.; Lu, J.; Hultman, L.; Rosen, J. Theoretical Stability and Materials Synthesis of a Chemically Ordered MAX Phase, Mo_2ScAlC_2, and Its Two-Dimensional Derivate Mo_2ScC_2 MXene. *Acta Mater.* **2017**, *125*, 476−480.
(61) Caspi, E. N.; Chartier, P.; Porcher, F.; Damay, F.; Cabioc'h, T. Ordering of (Cr,V) Layers in Nanolamellar $(Cr_{0.5}V_{0.5})_{n+1}AlC_n$ Compounds. *Mater. Res. Lett.* **2015**, *3* (2), 100−106.
(62) Liu, Z.; Zheng, L.; Sun, L.; Qian, Y.; Wang, J.; Li, M. $(Cr_{2/3}Ti_{1/3})_3AlC_2$ and $(Cr_{5/8}Ti_{3/8})_4AlC_3$: New MAX-Phase Compounds in Ti−Cr−Al−C System. *J. Am. Ceram. Soc.* **2014**, *97* (1), 67−69.
(63) Dahlqvist, M.; Rosen, J. Order and Disorder in Quaternary Atomic Laminates from First-Principles Calculations. *Phys. Chem. Chem. Phys.* **2015**, *17* (47), 31810−31821.
(64) Sang, X.; Xie, Y.; Lin, M.-W.; Alhabeb, M.; Van Aken, K. L.; Gogotsi, Y.; Kent, P. R. C.; Xiao, K.; Unocic, R. R. Atomic Defects in Monolayer Titanium Carbide ($Ti_3C_2T_x$) MXene. *ACS Nano* **2016**, *10*, 9193−9200.
(65) Halim, J.; Cook, K. M.; Eklund, P.; Rosen, J.; Barsoum, M. W. XPS of Cold Pressed Multilayered and Freestanding Delaminated 2D Thin Films of $Mo_2TiC_2T_z$ and $Mo_2Ti_2C_3T_z$ (MXenes). *Appl. Surf. Sci.* **2019**, *494*, 1138−1147.
(66) Chastain, J.; King, R. C.*Handbook of X-Ray Photoelectron Spectroscopy*; Perkin-Elmer Corporation, 1992; Vol. *40*, p 221.
(67) Halim, J.; Cook, K. M.; Naguib, M.; Eklund, P.; Gogotsi, Y.; Rosen, J.; Barsoum, M. W. X-Ray Photoelectron Spectroscopy of Select Multi-Layered Transition Metal Carbides (MXenes). *Appl. Surf. Sci.* **2016**, *362*, 406−417.
(68) Dahlqvist, M.; Alling, B.; Rosén, J. Stability Trends of MAX Phases from First Principles. *Phys. Rev. B: Condens. Matter Mater. Phys.* **2010**, *81* (22), 220102.
(69) Swalin, R. A.; Arents, J. Thermodynamics of Solids. *J. Electrochem. Soc.* **1962**, *109* (12), 308C.
(70) Dong, L.; Kumar, H.; Anasori, B.; Gogotsi, Y.; Shenoy, V. B. Rational Design of Two-Dimensional Metallic and Semiconducting Spintronic Materials Based on Ordered Double-Transition-Metal MXenes. *J. Phys. Chem. Lett.* **2017**, *8* (2), 422−428.
(71) He, J.; Ding, G.; Zhong, C.; Li, S.; Li, D.; Zhang, G. Cr_2TiC_2-Based Double MXenes: Novel 2D Bipolar Antiferromagnetic Semiconductor with Gate-Controllable Spin Orientation toward Antiferromagnetic Spintronics. *Nanoscale* **2019**, *11* (1), 356−364.
(72) Yang, C.; Jin, S. Z.; Liang, B. Y.; Jia, S. S. Low-Temperature Synthesis of High-Purity Ti_3AlC_2 by MA-SPS Technique. *J. Eur. Ceram. Soc.* **2009**, *29* (1), 181−185.
(73) Barsoum, M. W. *MAX Phases: Properties of Machinable Ternary Carbides and Nitrides*; John Wiley & Sons: NJ, 2013.

https://doi.org/10.1021/acsnano.1c02775
ACS Nano XXXX, XXX, XXX−XXX

(74) Van de Walle, A.; Tiwary, P.; De Jong, M.; Olmsted, D.; Asta, M.; Dick, A.; Shin, D.; Wang, Y.; Chen, L.-Q.; Liu, Z.-K. Efficient Stochastic Generation of Special Quasirandom Structures. *CALPHAD: Comput. Coupling Phase Diagrams Thermochem.* **2013**, *42*, 13−18.
(75) Perdew, J. P.; Burke, K.; Ernzerhof, M. Generalized Gradient Approximation Made Simple. *Phys. Rev. Lett.* **1996**, *77* (18), 3865.
(76) Kresse, G.; Hafner, J. *Ab Initio* Molecular Dynamics for Liquid Metals. *Phys. Rev. B: Condens. Matter Mater. Phys.* **1993**, *47* (1), 558.
(77) Kresse, G.; Furthmüller, J. Efficiency of *ab Initio* Total Energy Calculations for Metals and Semiconductors Using a Plane-Wave Basis Set. *Comput. Mater. Sci.* **1996**, *6* (1), 15−50.
(78) Kresse, G.; Furthmüller, J. Efficient Iterative Schemes for *ab Initio* Total-Energy Calculations Using a Plane-Wave Basis Set. *Phys. Rev. B: Condens. Matter Mater. Phys.* **1996**, *54* (16), 11169.
(79) Monkhorst, H. J.; Pack, J. D. Special Points for Brillouin-Zone Integrations. *Phys. Rev. B* **1976**, *13* (12), 5188.
(80) Manna, S.; Gorai, P.; Brennecka, G. L.; Ciobanu, C. V.; Stevanović, V. Large Piezoelectric Response of van der Waals Layered Solids. *J. Mater. Chem. C* **2018**, *6* (41), 11035−11044.

https://doi.org/10.1021/acsnano.1c02775
ACS Nano XXXX, XXX, XXX−XXX